*Progress In Electromagnetics Research M, Vol. 112, 67–80, 2022*

# Experimental Feasibility Study of Using mm-Wave for Arterial Radial Displacement Monitoring

**Somayyeh Chamaani[1, 2, *], Teresa Slanina[2], Duy Hai Nguyen[2], Jochen Moll[2], and Viktor Krozer[2]**

**Abstract**—Doppler Ultrasound as the gold standard for noninvasive arterial pulsation monitoring has limitations such as dependency on the operator and absence of acoustic window in some patients. Recently, mm-wave has been propounded as an alternative modality for biomedical diagnostics. However, heartbeat monitoring using mm-wave modality has been experimentally investigated only for external carotid artery, and its usage for deeper arteries has not been proved, yet. This study investigates the feasibility of mm-waves in the monitoring of non-superficial arteries. A continuous-wave (CW) reflectometer sensor is used for sensing pulsations exploiting the Doppler effect. The artery mimicking tube passes through an artificial agar-oil skin phantom. A peristaltic pump circulates the liquid through a tube. An antenna is placed in direct contact with the phantom without any coupling liquid. First, we investigate the optimum frequency of the given antenna in its impedance bandwidth [16 GHz–20 GHz]. Using the optimum frequency, the pulsation of an artery with a 1.6 mm diameter, placed in the depth of 16 mm, and has less than 0.02 mm radial oscillation amplitude was easily detectable.

## 1. INTRODUCTION

Monitoring of blood flow, wall displacement, and pressure pulse waves provide useful information in prediction, diagnostic and followup procedures by physicians [1–5]. Recent modalities for blood flow measurements are Doppler ultrasound, phase-contrast magnetic resonance imaging (PC-MRI), positron emission tomography (PET), photoplethysmography (PPG), laser Doppler, and laser speckle [6]. Among them, laser [2] and PPG [7–9] have very low penetration depth in the order of a few millimeters [10, 11]. The PC-MRI is very bulky and expensive, and PET is based on ionizing radiation. The Doppler ultrasound is the current gold standard for hemodynamic monitoring. However, the performance of Doppler ultrasound has some limitations, such as dependency on the operator [12, 13]. It also has limitations penetrating through bones [14–17], and, in some cases, osteoporosis presents a challenge due to scattering and multiple reflections [18], which makes it problematic for observing transcranial pulsations.

Electromagnetic waves as a different modality has been proposed for many medical sensing and imaging applications [12, 19–24]. Most of these researches are planned in the low microwave band, i.e., 1 GHz–4 GHz. Although low frequencies provide good penetration, higher frequencies have better sensitivity in their phase term. There are some studies about using higher frequencies for radar-based heartbeat detection in 16 GHz [25], and 24 GHz [26]. In [27–29], mechanical pulsations of the carotid artery, which is a significant big superficial artery, were monitored. To the best of our knowledge, a study of deeper arteries using an on-body sensor has not been performed yet.

*Received 14 March 2022, Accepted 24 June 2022, Scheduled 26 July 2022*

* Corresponding author: Somayyeh Chamaani (chamaani@kntu.ac.ir).

[1] Time-Domain Electromagnetics Laboratory, Faculty of Electrical Engineering, K.N. Toosi University of Technology, Tehran, Iran.

[2] Department of Physics, Goethe University of Frankfurt, Frankfurt, Germany.

This paper investigates the feasibility of using the mm-wave modality for arterial pulsation detection. The frequency is selected according to the optimum sensitivity of the antenna in the 16–20 GHz frequency range. Although this frequency range is below the standard mm-wave, the effective wavelength in the body is in the mm range. To detect the artery's pulsation, a single on-body antenna combined with a vector network analyzer (VNA) realizes a reflectometer sensor. The operating mode of VNA is continuous wave (CW). To mimic the pulsation of arteries, a peristaltic pump is used. Two silicon tubes with different internal diameters of 1.6 mm and 4.76 mm are used to simulate the arteries. Since about 80% of blood is water, we used water as the blood mimicking fluid. An artificial agar-oil phantom that mimics the skin dielectric properties surrounds the arteries. Different depths of artery — between 2 mm and 16 mm — are examined.

The rest of this paper is structured as follows. Section 2 describes materials and method, which includes sensing mechanism, experimental setup, antenna, and phantom. Section 3 focuses on results and discussion, and finally, Section 4 concludes the paper.

## 2. MATERIALS AND METHODS

### 2.1. Sensing Mechanism

As mentioned earlier, the current gold standard of arterial pulse wave monitoring is the Doppler ultrasound. Doppler ultrasound measures the blood flow velocity wave while reflectometer measures the radial displacement of the artery's wall. According to the simplified flow model in the artery [30], these two waves have similar periods. However, their waveform is different. The waveform of radial displacement is proportional to the pressure waveform. The radial displacement wave measurement has many applications, such as measuring the distensibility of the artery [31]. Combining these metrics, i.e., diameter and velocity waves also provides more accuracy in diagnosis [32]. The measured velocity of Doppler ultrasound is a function of angle and obeys the following equation:

$$u = \frac{v_0 f_d}{2 f_0 \cos\theta} \tag{1}$$

where $v_0$ is the speed of sound in the test tissue; $f_0$ is the frequency of transmitted ultrasound signal; and $f_d$ is the measured Doppler frequency due to the blood flow. The $\theta$ shows the angle between the ultrasound probe and artery (see Figure 1). According to (1), the Doppler velocity is a function of probe angle whereas, in normal incidence, no Doppler frequency will be measured. This is one of the limitations of handheld Doppler ultrasound devices, where choosing a proper angle needs the operator's expertise. In contrast, the mm-wave modality is less sensitive to the antenna's orientation, because it can be placed normal to the body surface which is very stable and does not need to be kept inclined by the operator. Indeed, since not all arteries are parallel with the body surface, the mm-wave sensor is also angle-dependent. However, this dependency will not lead to a blind angle, while the normal direction ($\theta = 90$), which is the most stable placement of the probe, sometimes corresponds to the blind angle of ultrasound. For better clarification, see the Figure 1(b). There exist numerous possibilities for orientations and without loss of generality, we have chosen here only three possible orientations for arteries beneath the skin. In all scenarios, antenna/ultrasound (US) probe is normal to the skin. Case (I), in which the artery is horizontal, the best direction for mm-wave is guaranteed. The case (I) is of course the blind angle for a normally directed Doppler ultrasound. In case (II), although the reflectometer receives less reflection from arteries wall, it still senses a fraction of wall displacement. This fraction is proportional to the projection of artery onto horizontal direction (dashed horizontal artery). The same argument is true for Doppler ultrasound where this time, the sensed velocity is proportional with projection of artery onto the vertical direction (dashed vertical artery). Case (III), where artery is normal to the skin, is the blind angle of reflectometer while it is the best angle for Doppler ultrasound. However, if we slightly move the antenna, it again becomes in the category of moderate angle which will have a horizontal component that can be sensed with the antenna (dashed antennas in case III). So, if we move slightly the antenna around a blind angle, the antenna will not be blind anymore. Note that in case (I), where we had blind angle for Doppler ultrasound, as long as the artery is in parallel with skin, moving the US probe will not remove the blindness. Moreover, it is worth noting that the case (III) is very rare in the arteries of human body where the case (I) is commonly found. So, the normal

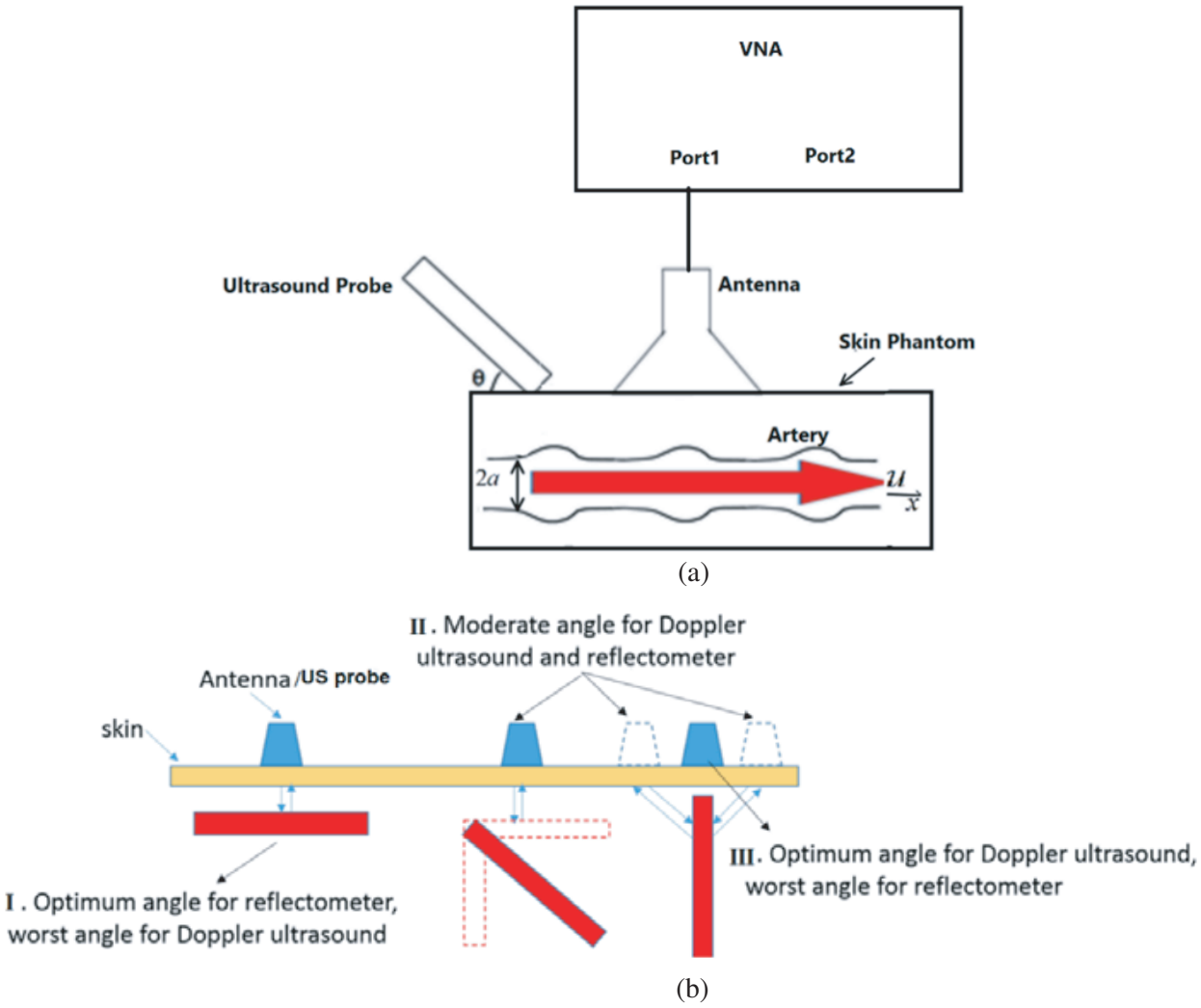


**Figure 1.** (a) The different sensing mechanisms of Doppler ultrasound and mm-wave sensor. Doppler ultrasound measures the blood flow velocity. Mm-wave reflectometer is implemented by only one port of VNA. It measures diameter variations of the artery — "$a$" stands for artery radius and "$x$" stands for blood flow direction, and (b) different orientations of artery and their effects on the sensing of a normally placed antenna/US probe to the skin.

placement of antenna which is more stable and reduces the operator dependency, is more consistent with mm-wave modality.

According to Figure 1(a), the mm-wave reflectometer is implemented by only one port of VNA. The measured $S_{11}$ includes contributions from the phase changes due to the antenna facing different tissue layers and due to arterial pulsation. Although both amplitude and phase of $S_{11}$ are sensitive to artery micro motions, the phase variations, especially in higher frequencies, are more significant. Therefore, we use phase of $S_{11}$ for pulsation monitoring. The phase of $S_{11}$ is separated into a static and a dynamic part:

$$\angle S_{11}(\tau) = \angle S_{110} + \angle S_{11a}(\tau) \tag{2}$$

where $\angle S_{110}$ is the static part due to antenna, cables, connectors, and the static contributions from the phantom. $\angle S_{11a}(\tau)$ is the dynamic part resulting from arterial pulsation over the observation time $\tau$. For the sake of simplicity, dynamic clutter signals have been ignored.

If we have a point target in free space and the far-field of an isotropic antenna, the reflected phase

due to the displacement of the target $\Delta a$ is:

$$\angle S_{11} = \frac{4\pi}{\lambda}\Delta a = \frac{4\pi}{c} f \Delta a \tag{3}$$

To choose the optimum frequency, we suppose that $\Delta a$ is constant (the target is motionless or the time is constant). In this case, the phase is a linear function of frequency, and the sensitivity to frequency is proportional to the constant value of $\frac{4\pi}{c}$. On the contrary, in our proposed system, the reflection coefficient phase is frequency-dependent. Because antennas and body tissues are dispersive (frequency-dependent); the antenna is not isotropic; the artery is not a point target and the tissue is in the antenna's near-field and loads the antenna. Therefore, there is no linear relation between phase and frequency like (3). Thus, we linearize the $\angle S_{11}$ using the mathematical definition of sensitivity $S_f$ as follows:

$$\angle S_{11} = S_f f \Delta a, \quad S_f = \frac{\partial \angle S_{11}}{\partial(\Delta a f)} = \frac{1}{\Delta a}\frac{\partial \angle S_{11}}{\partial f} \tag{4}$$

Consequently, the time variant phase of reflection coefficient can be written as:

$$\angle S_{11}(\tau) = S_f f K_0 + S_f f \Delta a(\tau) \tag{5}$$

where $\Delta a(\tau)$ shows displacement of artery's wall over the time, and $S_f$ is sensitivity factor with respect to the frequency for a constant value of $\Delta a$ and $K_0$ is a constant. $S_f f K_0$ is related to the static part of $\angle S_{11}$ and is ignored for arterial pulsation monitoring.

Since we suggest operating in CW mode, $S_f f$ will be constant during the pulsation capturing. However, we can choose the frequency with the maximum value of $S_f$ to get the best sensitivity. This usually happens in the resonance frequency of the sensing system which has a sharp phase response. More detail will be given in Subsection 3.1.

### 2.2. Experimental Setup

The experimental setup is shown in Figure 2(a). Two tubes with different diameters are placed in a plastic container. Since the pump has only one head, only one of the tubes can work at each time. The water, as blood mimicking fluid, comes from the reservoir to the peristaltic pump and after the pump, goes to the phantom. The output of the phantom comes back through another tube to the reservoir. The direction of flow is shown using arrows in Figure 2(a). The pump contracts the tube periodically and mimics the arterial pulsations. An antenna is placed in contact with the phantom. An HP 8720 VNA works in CW mode in the time domain and records the amplitude and phase of the reflection coefficient of the antenna over the pulsation of the artery.

The box including the tubes before filling with phantom is shown in Figure 2(b). A photograph of the system is shown in Figure 2(c). The pump is LA-900 pump from HLL (Landgraf Laborsystem) [33]. The control signal of pump is on/off (pulse) with tunable level and delay between sequential pulses. Depending on the relaxation time of system and period of pulse, different waveforms are obtained. The selected period is 1.8 s which leads to the pulsation frequency of 0.55 Hz. A laser is also applied to measure the amount of arterial diameter variations. Since the laser cannot penetrate through the phantom material, measurement of artery's diameter variation inside the phantom is not possible. Therefore, we placed laser outside the phantom (over the green grip tape in Figure 2(c)). Of course this variations is larger than the diameter variations inside the phantom. The tubes pass through the skin phantom. An antenna is placed directly on the phantom and is connected with a coaxial cable to the VNA. The details of antennas and phantom are described in the following subsections.

### 2.3. Antenna Structure

An ultra-wideband (UWB), planar, bowtie-liked patch antenna structure is proposed for this work, as shown in Figure 3. According to the figure, a radiating element and its input power network are integrated on the same substrate (Rogers RO4350B $\varepsilon_r = 3.55$ at 10 GHz [34]), thanks to the multi-layer technology. A common ground layer L3 is deployed to separate the structures and enhancing the isolation between components in the design. Thus, it is possible to design the radiating and feeding elements individually and the integration of both is straightforward. In the design, substrate thickness

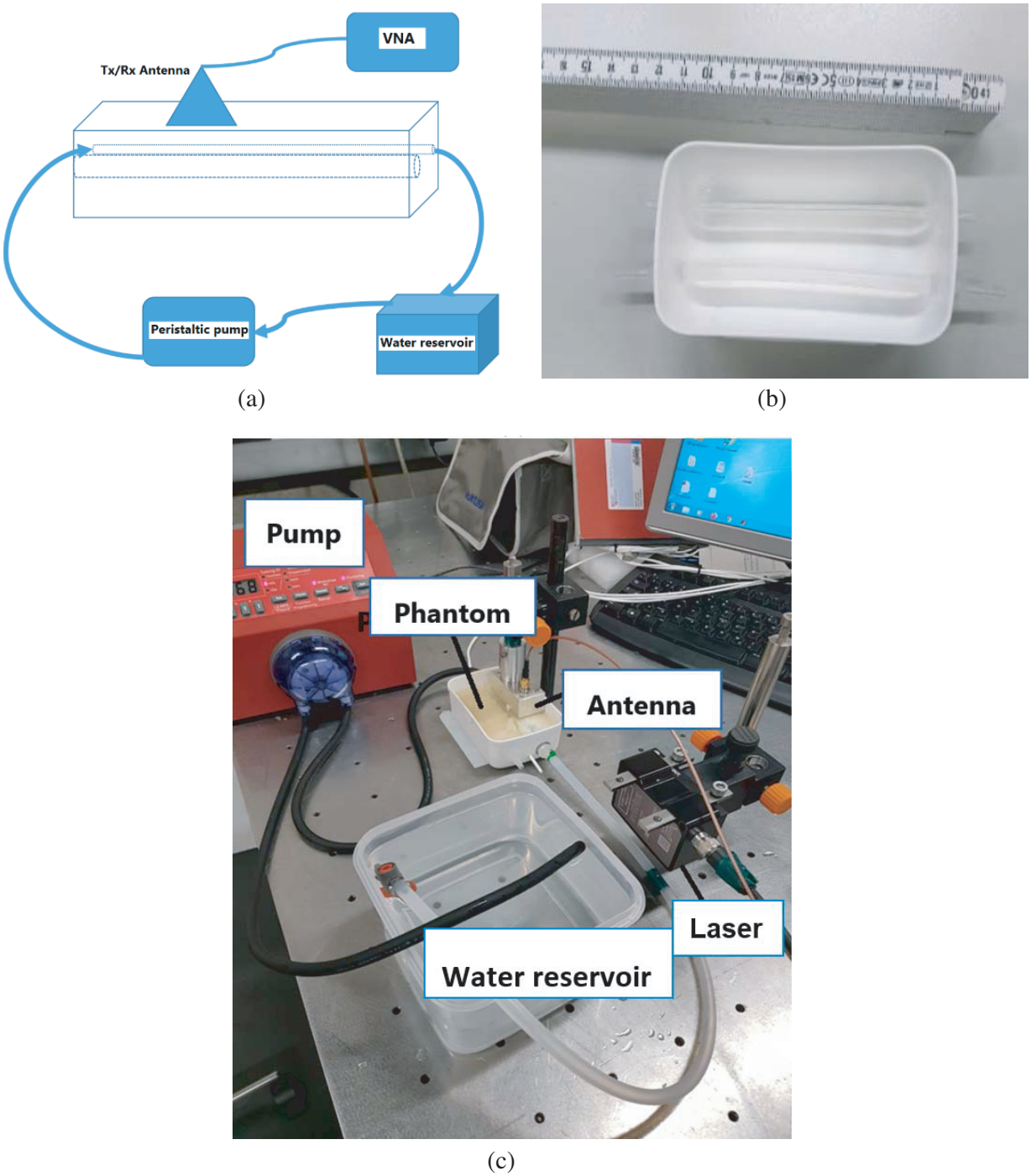


**Figure 2.** (a) Schematic of measurement scenario, (b) the box including two tubes mimicking two different size of arteries. This box will be filled with skin mimicking phantom material, and (c) implemented measurement set up.

of the radiating element (TOP-L3) and power excitation network (L3-BOT) is $h_{antenna} = 0.9\,\text{mm}$ and $h_{feed} = 0.3\,\text{mm}$, respectively. At high-frequency ranges, microwave signals are affected by significant power attenuation when propagating inside the biological tissue [35]. For this reason, the main radiating patches are designed at the L2 layer to fully establish radiation characteristics before entering the tissue. Our simulations show that the edge corrugations of the patches improve the antenna's bandwidth,

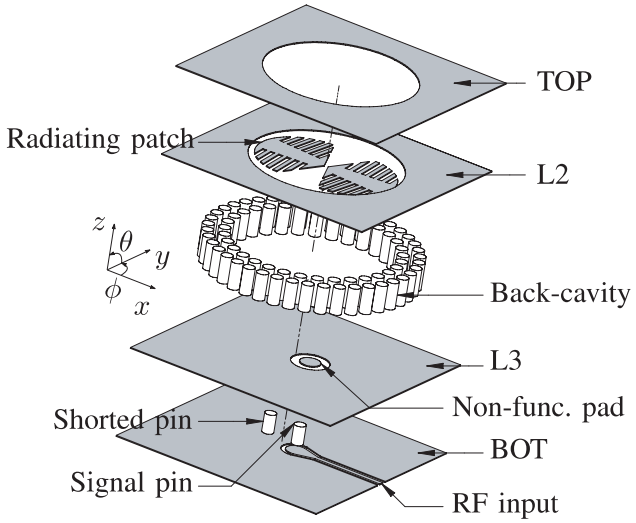


**Figure 3.** Schematic overview of the antenna structure and its technology. For simplicity, substrate Rogers RO4350B is not shown.

especially in the lower frequency ranges. The radiating patches are excited by transmission pins connected to the antenna input at the BOT layer. Here, an asymmetrical feeding mechanism is used, in which one signal pin is shorted to the ground to maintain a compact design. Also, due to manufacturing rules, pads are adopted to ensure the connection of the feeding pins in each layer. Finally, a back cavity, implemented via holes, is used to improve the antenna's characteristics by suppressing surface wave propagation inside planar structures [36].

The proposed antenna is realized, which is shown in Figure 4.

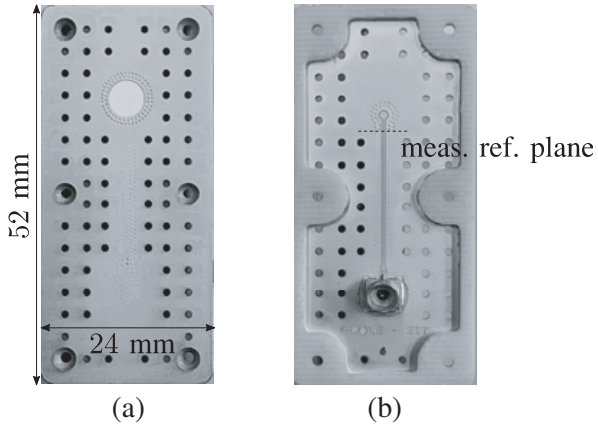


**Figure 4.** Photographs of the antenna prototype. (a) Top view. (b) Bottom view.

### 2.4. Phantom

Since the body's first layer is skin, we used skin phantom as a preliminary experiment. More realistic multilayer phantoms will be used in the future. The utilized skin phantom comprises distilled water, glycerin, agar, rapeseed oil, and dishwashing liquid. To prepare the phantom, 165 ml distilled water, and 52.5 ml glycerin must be mixed, then 20.4 g agar should be added. Subsequently, the mixture has to be heated up to 63°C, while it is continuously stirred with a stirrer and a magnetic stir fish. When the mixture reaches 63°C, the rapeseed oil can be added slowly. Overall, 150 ml of rapeseed oil has to be added. The temperature should remain above 50°C. When the whole oil is added, and the temperature

reaches 63°C, the 9 ml dishwashing liquid can be added. Now the stirrer can be stopped and stirred by hand until the emulsion is homogeneous. Now the phantom can be filled in the box and cooled down overnight. The measurement of the relative permittivity with an open-ended coaxial probe in the frequency range from 50 MHz up to 20 GHz is shown in Figure 5. The real part of the relative permittivity is 13.5, and the imaginary part of the relative permittivity is 7.4 at 17 GHz.

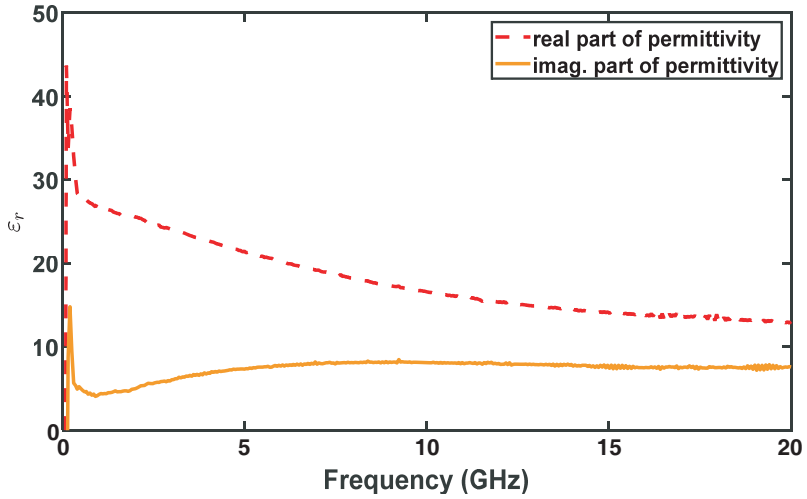


**Figure 5.** The measured relative permittivity of the skin phantom at room temperature.

## 3. RESULTS AND DISCUSSION

### 3.1. Best CW Frequency Selection

Although the antenna's bandwidth is very wide [37], due to high penetration loss above 20 GHz, we limit the test to the frequency range of 16–20 GHz. As pointed out in Subsection 2.1, the optimum frequency of operation for the CW sensor, which provides maximum sensitivity, should be determined first. Since the antenna needs the body tissue as a matching layer, its response is sensitive to the body tissue's characteristics and thickness. Therefore, we measured the reflection coefficient of the antenna over the specific phantom used in this paper for different thicknesses of phantoms. The results of the two exemplar thicknesses are shown in Figure 6(a). As observed, the antenna is best matched around 17.4 GHz. We also see a fast variation of phase in Figure 6(b). Indeed, this sharp change of the phase of $S_{11}$ provides maximum sensitivity according to Eq. (4). The sensitivity for Figure 6(b) is depicted in Figure 7, which shows the maximum sensitivity around 17.4 GHz. Therefore, this frequency was selected as the frequency of the CW reflectometer. It is worth mentioning that in CW mode, we are using the phase to capture the arterial wall micromotions.

For better illustration, captured phases over the observation time at different frequencies are shown in Figure 8 (Phantom's thickness = 5.5 mm). As observed, the maximum variation of phase is obtained at 17.4 GHz.

The angular dependency of the reflectometer sensor is investigated by rotating the antenna in directions shown in Figure 9. The pulsations captured in the phase of reflection coefficient are depicted in Figure 10. All these measurements are performed at 17.4 GHz. As observed, pulsation is detectable in all angles. This is against the ultrasound modality in which the pulsation is detectable only in very limited angles. It is worth mentioning that the thickness and age of the phantom and also the pulsation amplitude used in Figure 10 are different from those used in Figure 8. Therefore, the quantitative values of arterial pulsation amplitude should not be compared in these two figures.

All the reported results until now belonged to the big artery with the internal diameter of 4.76 mm and wall thickness of 1.5 mm. We have also measured the pulsation of the small artery model with an inner diameter of 1.6 mm and wall thickness of 1.5 mm. The center of the artery representing the tube

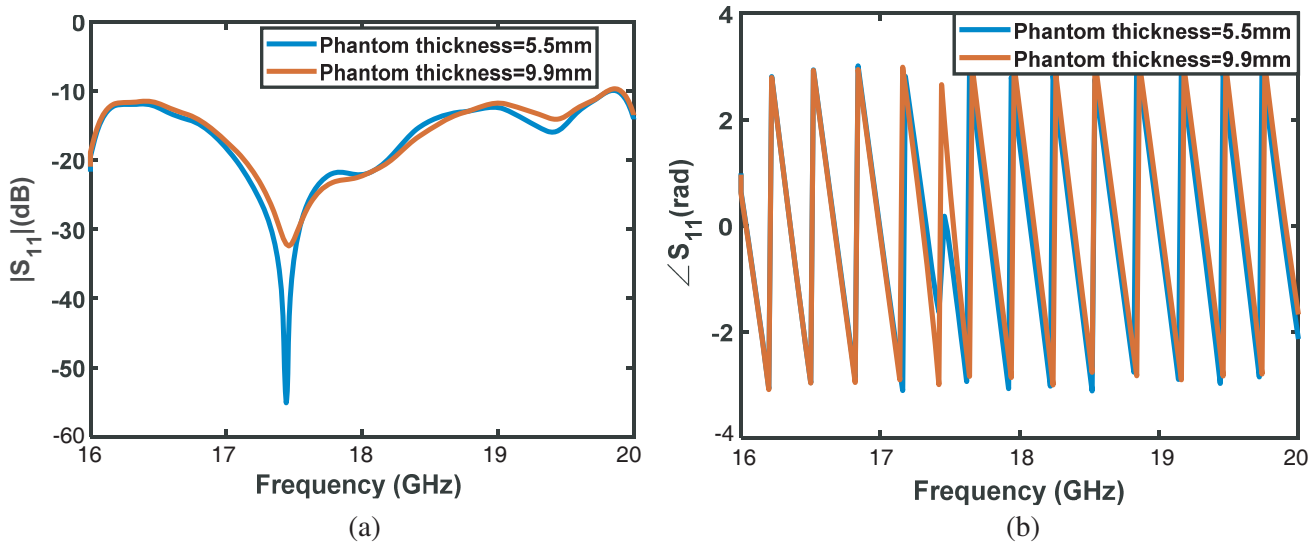


**Figure 6.** (a) Measured magnitude of the reflection coefficient of antenna over two different phantom thicknesses, (b) measured phase of the reflection coefficient of the antenna over two different thicknesses of phantom. In measurements, there is a sharp variation of antenna phase response around 17.4 GHz. This frequency is the optimum frequency for capturing small arterial wall displacements.

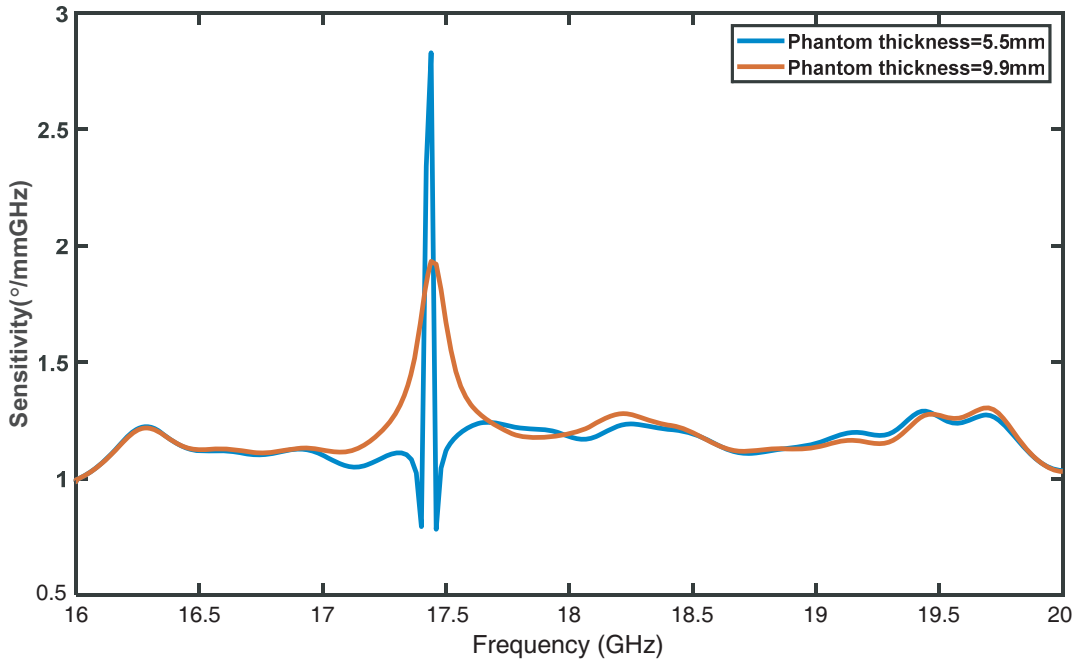


**Figure 7.** Sensitivity of the phase response of antenna placed over the phantom in a monostatic scenario (reflectometer).

is placed at a depth of 16 mm from the surface of the phantom. The laser indicates a radius variation of 0.02 mm for this artery model. Obviously, the displacement is smaller in the phantom. The antenna is placed at an angle of 0° (see Figure 9). As seen in Figure 11, the pulsation is easily detectable for this small artery, despite the very small displacement values. To calculate the signal to noise ratio (SNR)

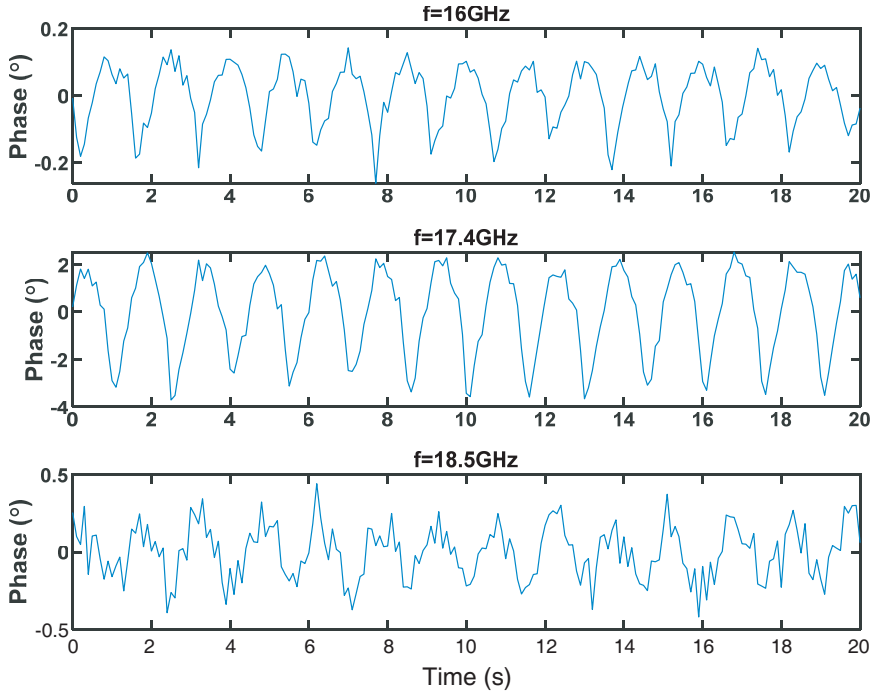


**Figure 8.** Dynamic part of captured $\angle S_{11}$ of reflectometer above the pulsating artery in different frequencies.

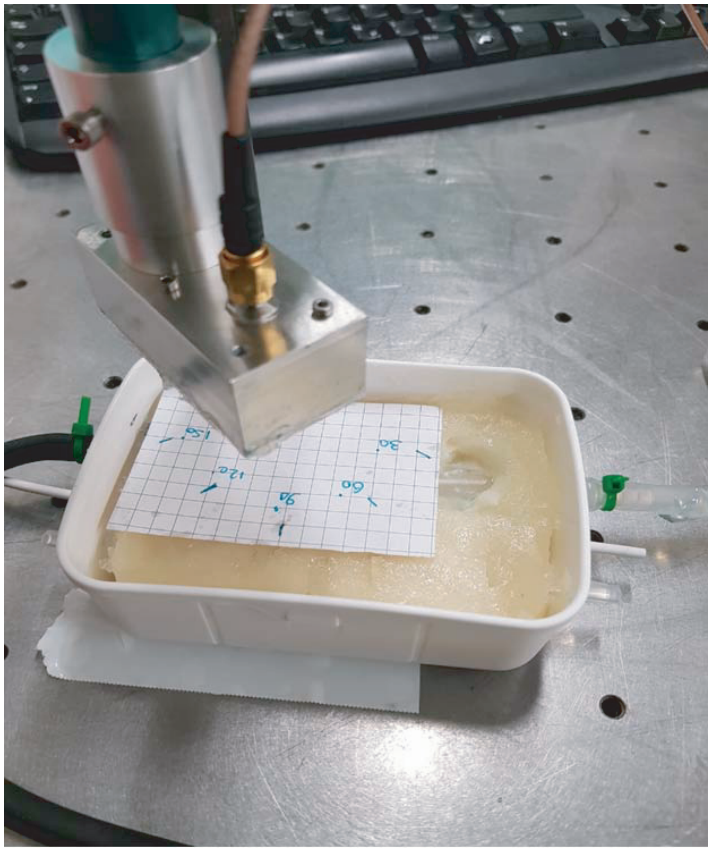

**Figure 9.** The antenna rotates in predefined directions.

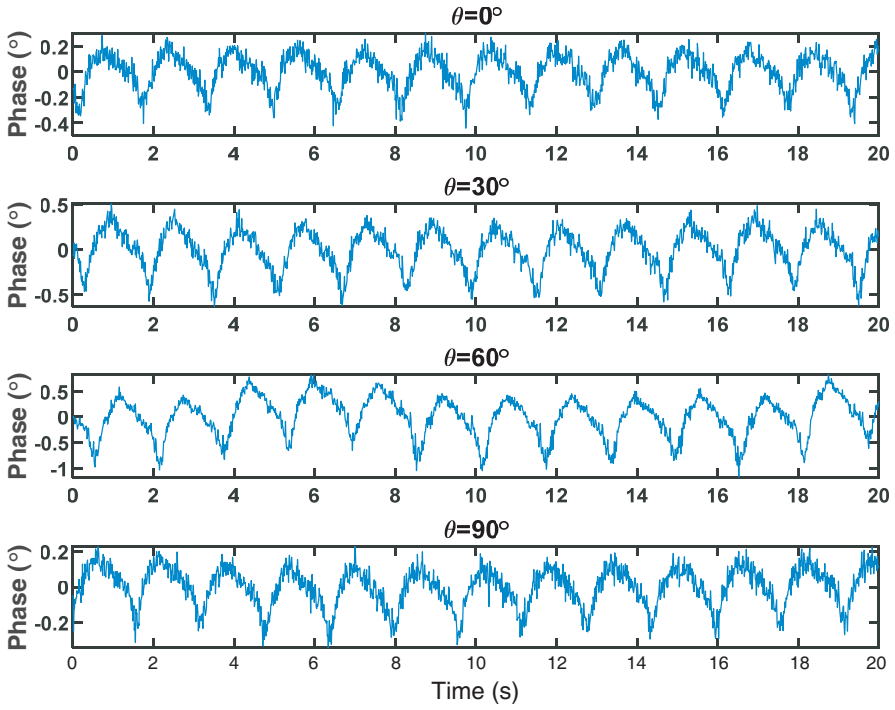


**Figure 10.** The pulsations captured by the antenna at 17.4 GHz for different angular orientations of the antenna.

in this measurement, the following formula is used [38]:

$$SNR_{dB} = 20 \log \left( \frac{\Delta P}{V_n} \right) \tag{6}$$

where $\Delta P$ is the peak-to-peak value of the phase signal (filtered), and $V_n$ is the RMS (root mean square) value of the noise, measured when the artery is not pulsating.

$V_n$ is 0.1°. The $\Delta P$ in Figure 11 is 0.8° which leads to 18 dB SNR.

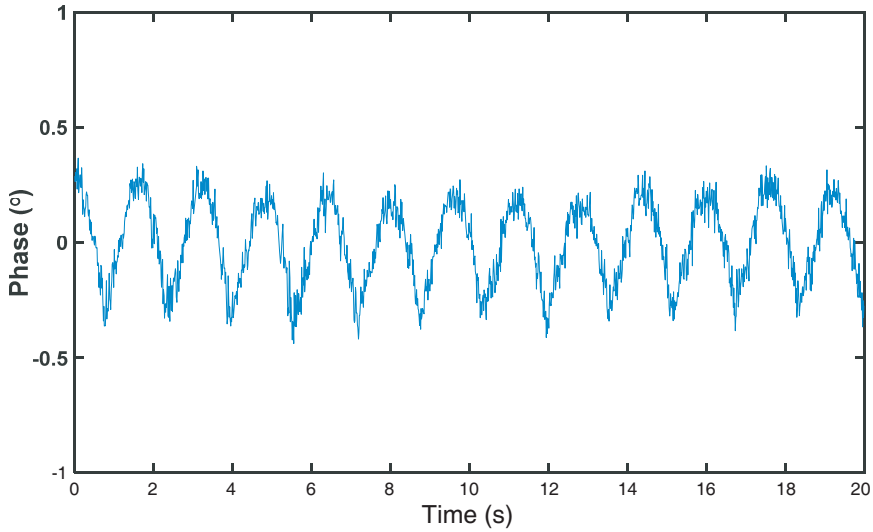


**Figure 11.** Pulsation wave of small artery in the depth of 16 mm, acquired by CW reflectometer in 17.4 GHz.

### 3.2. Cross Range Resolution

The antenna's footprint dictates the ability of a CW reflectometer to resolve between two adjacent arteries. Therefore, we simulated the antenna's footprint in the resonance frequency (Figure 12). If we want to resolve two parallel arteries lying in the $y$-direction, the antenna's beamwidth in the $x$-direction is determinative. Thanks to the high frequency of mm-wave which leads to high loss in the body, the footprint is nicely focused. Looking at Figure 12(c), the antenna beamwidth in the $x$-direction is a function of depth ($z$). Two exemplar $x$-direction beamwidth in different depths are listed in Table 1. It is seen that for arteries placed in depth $h2$ (8.3 mm), the top parts of the left and right arteries (dashed lines),which are placed in the cyan part of footprint, experience about 15 dB attenuation with respect to the artery placed in boresight of antenna (placed in the yellow part of footprint). It means, they experience $2*15 = 30$ dB more attenuation in the reflection coefficient. So they are completely resolvable. Depending on the receiver threshold, the resolution might be even better, e.g., for conventional CW radar applications, 3 dB beamwidth of antenna is the criterion for cross range resolution. To further improve the resolution, we would need a more focused antenna. The optimum design of the antenna is the topic of our future research.

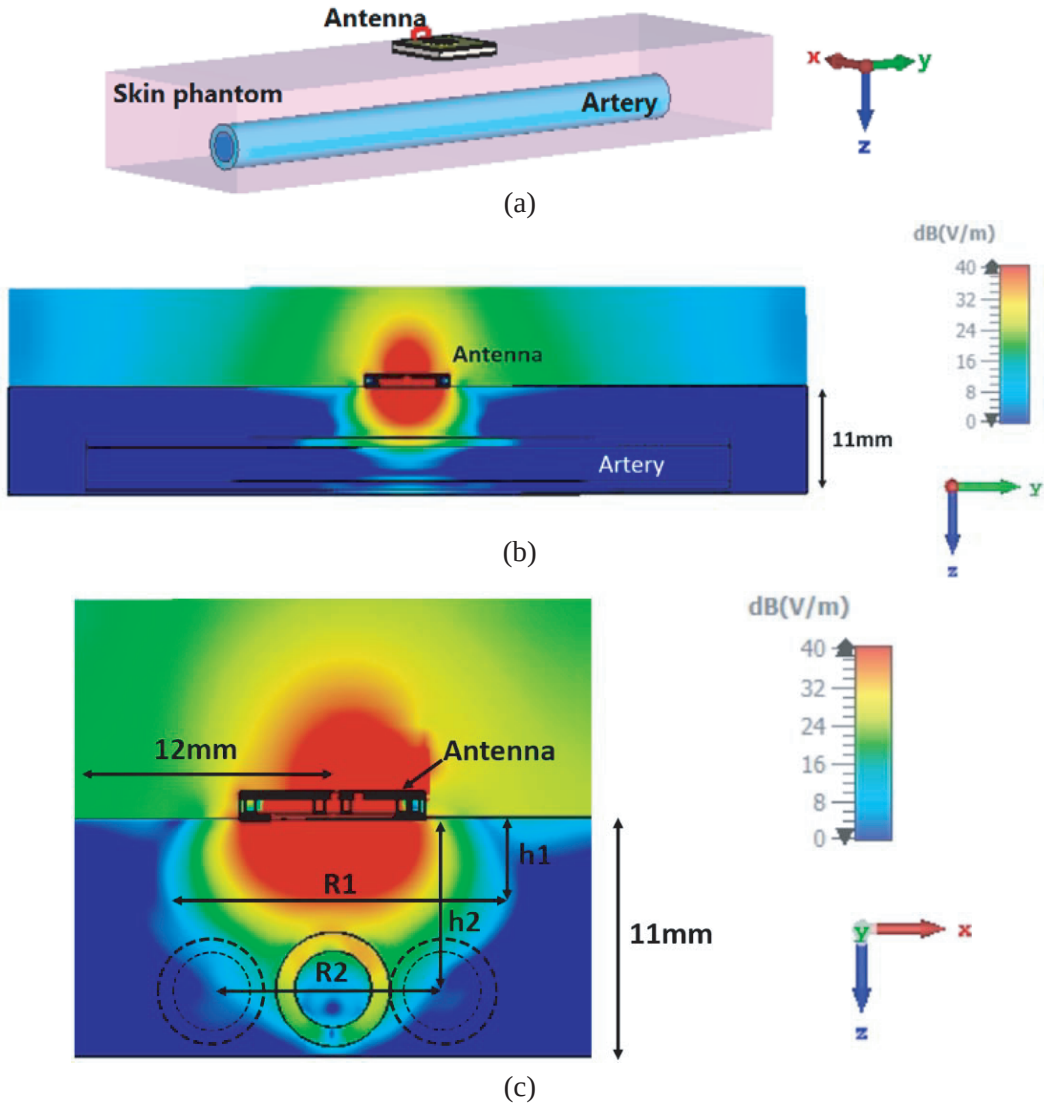


**Figure 12.** Simulation results of penetration of the antenna's electric field inside the phantom. (a) Simulation setup, (b) electric field pattern in the $yz$-plane, and (c) electric field pattern in the $xz$-plane.

**Table 1.** Antenna's $x$-direction beamwidth in different depths (see Figure 12).

| Ordered pair | Value (mm) |
|---|---|
| $(h1, R1)$ | (4.3, 14.4) |
| $(h2, R2)$ | (8.3, 7) |

## 4. CONCLUSIONS

It was shown that radial displacement waves of arteries could be captured using a CW reflectometer. The mm-wave band was used for non-superficial arterial pulsation monitoring for the first time. It was shown that the antenna over the phantom has to resonate in the reflectometer's frequency to obtain the optimum sensitivity. It was observed that the wall displacement waveform captured by the mm-wave reflectometer is easily detectable for arteries with a 1.6 mm diameter and in the depth of 16 mm. Against the Doppler ultrasound, which needs inclined contact with the body, the reflectometer should be placed normally on the body. This normal placement decreases the dependency of results on the inclined angle and reduces the unwanted effects from the operator's hand movement. The angular dependency of the reflectometer sensor in the azimuth plane was also very low. Therefore, mm-wave is a promising modality that can be used as a stand-alone or an adjoint sensor for arterial waveform sensing. Future steps could be investigating the maximum achievable depth and penetrating through the bones.

## ACKNOWLEDGMENT

This work has been supported by the project Indi Thera (13GW0361D) through the Federal Ministry of Education and Research (BMBF) and project FEDORA (464551671) from the German Research Foundation.

Authors would like to thank Jonathan Stindl for his helpful support.

## REFERENCES

1. Routh, H. K., "Doppler ultrasound," *IEEE Eng. Med. Biol.*, No. 3, 1996.
2. Li, Y., P. Segers, J. Dirckx, and R. Baets, "On-chip laser Doppler vibrometer for arterial pulse wave velocity measurement," *Biomed. Opt. Express*, Vol. 4, No. 7, 1229–1235, 2013.
3. Sun, C.-K., "Cardio-ankle vascular index (CAVI) as an indicator of arterial stiffness," *Dovepress*, No. 6, 27–38, 2013.
4. Boutry, C. M., et al., "Biodegradable and flexible arterial-pulse sesnor for the wireless monitoring of blood flow," *Nat. Biomed. Eng.*, Vol. 3, No. 1, 2019.
5. Avolio, A. P., M. Butlin, and A. Walsh, "Arterial blood pressure measurement and pulse wave analysis — Their role in enhancing cardiovascular assessment," *Physiol. Meas.*, Vol. 31, 1–47, 2010.
6. Jayanthy, A. K., N. Sujatha, and M. R. Reddy, "Measuring blood flow: Techniques and applications — a review," *Int. J. Res. Rev. Appl. Sci.*, Vol. 6, No. 2, 203–216, 2011.
7. Saugel, B., et al., "Cardiac output estimation using pulse wave analysis d physiology, algorithms, and technologies: A narrative review," *Br. J. Anaesth.*, Vol. 126, No. 1, 67–76, 2021.
8. Saugel, B., et al., "Continuous noninvasive pulse wave analysis using finger cuff technologies for arterial blood pressure and cardiac output monitoring in perioperative and intensive care medicine: A systematic review and meta-analysis," *Br. J. Anaesth.*, Vol. 125, No. 1, 25–37, 2020.
9. Elgendi, M., et al., "The use of photoplethysmography for assessing hypertension," *NPJ Digit. Med.*, Vol. 60, 1–11, 2019.
10. Johansson, K., H. Ahn, J. Lindhagen, and O. Lundgren, "Tissue penetration and measuring depth of laser Doppler flowmetry in the gastrointestinal application," *Scand. J. Gastrology*, Vol. 22, No. 9, 1081–1088, 2009.

11. Chatterjee, S., J. P. Phillips, and P. A. Kyriacou, "Monte Carlo investigation of the effect of blood volume and oxygen saturation on optical path in reflectance pulse oximetry," *Biomed. Phys. Eng. Express*, Vol. 2, No. 6, 1–14, 2016.
12. Ruvio, G., A. Cuccaro, R. Solimene, A. Brancaccio, B. Basile, and M. J. Ammann, "Microwave bone imaging: A preliminary scanning system for proof-of-concept," *Healthc. Technol. Lett.*, Vol. 3, No. 3, 218–221, 2016.
13. Quail, A. W., D. B. F. Cottee, and S. W. White, "Limitations of a pulsed Doppler velocimeter for blood flow measurement in small vessels," *J. Appl. Physiol.*, Vol. 75, No. 6, 2745–2754, 1993.
14. Libove, J., D. Schriebman, and M. Ingle, "Picosecond pulse imaging — Uniquely promising but challenging modality for a wearable BMI," *2017 IEEE International Conference on Systems, Man, and Cybernetics (SMC)*, 2448–2453, 2017.
15. Libove, J., D. Schriebman, M. Ingle, and B. Wahl, "Wearable brain imager/BMI technology for structural, vascular and functional extraction," *2016 IEEE International Conference on Systems, Man, and Cybernetics (SMC)*, 3806–3811, 2016.
16. Deverson, S., D. H. Evans, and D. C. Bouch, "The effects of temporal bone on transcranial Doppler ultrasound beam shape," *Ultrasound Med. Biol.*, Vol. 26, No. 2, 239–244, 2000.
17. Zhou, T., S. Member, P. M. Meaney, M. J. Pallone, S. Geimer, and K. D. Paulsen, "Microwave tomographic imaging for osteoporosis screening: A pilot clinical study," *IEEE Eng. Med. Biol. Soc. 2010*, 1218–1221, 2010.
18. Michimoto, I., et al., "Simulation study on the effects of cancellous bone structure in the skull on ultrasonic wave propagation," *Sci. Rep.*, Vol. 11, No. 1, 1–12, 2021.
19. Chandra, R., H. Zhou, I. Balasingham, S. Member, and R. M. Narayanan, "On the opportunities and challenges in microwave medical sensing and imaging," *IEEE Trans. Biomed. Eng.*, Vol. 62, No. 7, 1667–1682, 2015.
20. Meaney, P. M., et al., "Clinical microwave tomographic imaging of the calcaneus: A first-in-human case study of two subjects," *IEEE Trans. Biomed. Eng.*, Vol. 59, No. 12, 3304–3313, 2012.
21. Amin, B., M. A. Elahi, A. Shahzad, E. Porter, B. McDermott, and M. O'Halloran, "Dielectric properties of bones for the monitoring of osteoporosis," *Med. Biol. Eng. Comput.*, Vol. 57, No. 1, 1–13, 2019.
22. Amin, B., A. Shahzad, M. O'halloran, and M. A. Elahi, "Microwave bone imaging: A preliminary investigation on numerical bone phantoms for bone health monitoring," *Sensors (Switzerland)*, Vol. 20, 1–21, 2020.
23. Mase, A., et al., "Non-contact and real-time measurement of heart rate and heart rate variability using microwave reflectometry," *Rev. Sci. Instrum.*, Vol. 91, No. 1, 2020.
24. Nagae, D. and A. Mase, "Measurement of heart rate variability and stress evaluation by using microwave reflectometric vital signal sensing," *Rev. Sci. Instrum.*, Vol. 81, No. 9, 2010.
25. Dany Obeid, G. E. Z., G. Zaharia, and S. Sadek, "Microwave Doppler radar for heartbeat detection vs electrocardiogram," *Microw. Opt. Technol. Lett.*, Vol. 54, No. 11, 2610–2617, 2013.
26. Xu, Y., Q. Li, and Z. Tang, "Accurate and contactless vital sign detection in short time window with 24 GHz Doppler radar," *J. Sensors*, Vol. 2021, 1–14, 2021.
27. Shi, K., S. Schellenberger, T. Steigleder, F. Michler, and F. Lurz, "Contactless carotid pulse measurement using continuous wave radar," 1–3, November 2018.
28. Chamaani, S., A. Akbarpour, M. Helbig, and J. Sachs, "Matrix pencil method for vital sign detection from signals acquired by microwave sensors," *Sensors*, Vol. 21, No. 17, 1–24, 2021.
29. Pisa, S., S. Chicarella, E. Pittella, E. Piuzzi, O. Testa, and R. Cicchetti, "A double-sideband continuous-wave radar sensor for carotid wall movement detection," *IEEE Sens. J.*, Vol. 19, No. 10, 8162–8171, 2018.
30. Fung, Y. C. and S. C. Cowin, *Biomechanics: Motion, Flow, Stress, and Growth*, 1st Edition, Springer, New York, 1990.
31. Hoeks, A. P. G., P. J. Brands, F. A. M. Smeets, and R. S. Reneman, "Assesment of the distinsibility of superficial arteries," *Ultrasound Med. Biol.*, Vol. 16, No. 2, 121–128, 1990.

32. Mynard, J. P., A. Kondiboyina, and R. Kowalski, "Measurement, analysis and interpretation of pressure/flow waves in blood vessels," *Front. Physiol.*, Vol. 11, 1–26, 2020.
33. "A-900 Peristaltic pump", [Online], Available, https://www.hll.de/12/1/AD223/MTA2NzIwNDA-w/Landgraf HLL 106720400 Landgraf HLL.html.
34. R. Corporation, "RO4000® Series High Frequency Circuit Materials," 2018.
35. Nikolova, N. K., "Microwave imaging for breast cancer," *IEEE Microw. Mag.*, Vol. 12, No. 7, 78–94, 2011.
36. Nguyen, D. H., J. Ala-laurinaho, J. Moll, V. Krozer, and S. Member, "Improved sidelobe-suppression microstrip patch antenna array by uniform feeding networks," *IEEE Trans. Antennas Propag.*, Vol. 68, No. 11, 7339–7347, 2020.
37. Nguyen, D. H., J. Moll, V. Krozer, V. Memmolo, and G. Zimmer, "Elliptical monopole antenna design for the early breast cancer imaging at high frequencies," *2021 15th European Conference on Antennas and Propagation (EuCAP)*, 1–4, 2021.
38. Scalise, L., A. De Leo, V. Mariani Primiani, P. Russo, D. Shahu, and G. Cerri, "Non contact monitoring of the respiration activity by electromagnetic sensing," *MeMeA 2011 — 2011 IEEE Int. Symp. Med. Meas. Appl. Proc.*, 418–422, May 2011.